**Noname manuscript No.**
(will be inserted by the editor)

# Application of a Variational Approach to the Computation of Forces around a Wing

**Daniel Díaz-Arriba · Bartosz Protas · Gwenaël Acher · Frédéric Pons · Laurent David**

Received: date / Accepted: date

**Abstract** In this paper we present an application of the variational approach, introduced by Quartapelle & Napolitano (1983) and developed further by Protas et al. (2000), which requires only the velocity fields and its derivatives to determine forces acting on a body. First, the approach is presented and adapted to our 3D test problem. The obtained expression for the hydrodynamic force involves a harmonic function $\eta$ whose determination is also presented. Then, numerical flow fields obtained with LES are used in order to evaluate the influence of different parameters on the forces and to offer a validation of the proposed approach. This allows us to assess the accuracy of the method and its advantages.

Next, a comparison of the proposed variational approach with the momentum equation approach presented by David et al. (2009) is discussed. The momentum equation approach offers a non-intrusive method to determine forces, but requires the pressure field around the object. On the other hand, the variational approach requires the determination of the vorticity field on the surface of the wing, which is not always trivial to obtain with sufficient accuracy, but the computation of the pressure field can be avoided. This paper aims to compare both methods in a practical setting and show their relative advantages and sensitivities to different parameters for a 3D numerical/experimental study of a flow field around a NACA0015 airfoil. To the best of our knowledge, this is the first application of the variational approach in an experimental setting.

**Keywords** Non-intrusive Methods · Force Determination · Variational approach · 3D velocity field

D. Diaz-Arriba
Institut Pprime CNRS, Univerité Poitiers, ENSMA, France
Tel.: +33666632427
E-mail: dani.diaz.arriba@gmail.com
*Present address: ISAE-Supaero, Toulouse University, France*

B. Protas
Department of Mathematics & Statistics, McMaster University, Hamilton, Ontario, Canada

G. Acher, F. Pons, L. David
Institut Pprime CNRS, Univerité Poitiers, ENSMA, France

## 1 Introduction

Non-intrusive determination of aerodynamic forces experienced by a body has become an important topic of research in the last years. Low Reynolds number flows that involve weak forces, such as flows around nano-air vehicles (NAVs), may benefit from the use of non-intrusive methods to obtain reliable results. Direct measurements of forces are not always feasible and it is particularly difficult to obtain the correlation between forces and vortex structures (Jardin et al., 2009).

Unal et al. (1997) introduced the first non-intrusive method discussed in this paper which derives unsteady forces from velocity fields by the application of the momentum equation to a control volume around the body. This method allows for the determination of steady (Van Oudheusden et al., 2006) and unsteady (Kurtulus et al., 2007) aerodynamic forces. Moreover, David et al. (2009) developed some practical applications of this approach for numerical and experimental data in 2D. Nevertheless, the momentum equation approach has its drawbacks, such as the presence of terms involving pressure which have to be evaluated on the boundaries of the control volume (for 3D flows, this requires pressure fields available at the boundary surfaces) or the sensitivity to the chosen control volume. This motivates the development of alternative non-intrusive methods that would not suffer from these drawbacks.

Another family of methods of force determination relies on the impulse equation initially developed by Lin & Rockwell (1996) and then extended to control volumes by Noca et al. (1997, 1999). A recent account of this method was presented by Lighthill (1986). The impulse approach allows for the calculation of the force using expressions based on the velocity and vorticity fields only. Comparison between the two approaches showed a good agreement of the results (Noca et al., 1997, 1999). Nevertheless, the impulse method is sensitive to the noise, affecting the vorticity evaluation as it has been shown recently by (Limacher et al., 2020).

With the same objective of eliminating the need to compute pressure when determining forces, Protas et al. (2000) assessed the effectiveness of the variational approach initially proposed by Quartapelle & Napolitano (1983) on 2D numerical data and showed good accuracy of results for flows at a low Reynolds number. Various aspects of the variational approach were developed by Chang (1992); Howe (1995); Chang and Lei (1996); Chang, Su, and Lei (1998); Pan and Chew (2002). In this paper, we revisit the variational approach and extend it to 3D flows in realistic settings and at high Reynolds numbers. In addition, the influence of key parameters such as the spatial resolution and the size of the integration domain on the accuracy of the computed forces will be carefully assessed using a numerical database. Then, a comparison between the variational and the momentum equation approaches will be presented based on both numerical and experimental data, leading to a concluding discussion. To the best of our knowledge, this is the first investigation where the variational approach is used to determine the hydrodynamic force based on experimental flow measurements.

## 2 Methods of force determination

### 2.1 Momentum equation approach

Practical application of the momentum equation approach is possible thanks to the determination of the velocity and acceleration fields using Time-Resolved Particle Image Velocimetry (TR-PIV). This approach provides the following integral expression for the instantaneous force $\vec{F}(t)$ on the body

$$\vec{F}(t) = -\rho \iiint_{\Omega} \frac{\partial \vec{V}}{\partial t}\, d\Omega - \rho \iint_{\Gamma_1} \left(\vec{V}\cdot\vec{n}\right)\left(\vec{V}-\vec{V}_s\right) d\sigma - \iint_{\Gamma_1} p\,\vec{n}\, d\sigma + \iint_{\Gamma_1} \overline{\overline{\tau}}\cdot\vec{n}\, d\sigma, \tag{1}$$

where $\vec{n}$ is the normal vector to the control surface $\Gamma_1$ as shown in Figure 1, $\rho$ is the fluid density, $\vec{V}$ is the fluid velocity field, $\vec{V}_s$ is the velocity of the boundary of the control volume and

$$\overline{\overline{\tau}} = \mu\left[\vec{\nabla}\vec{V} + \vec{\nabla}\left(\vec{V}\right)^t\right] \tag{2}$$

is the viscous stress tensor.

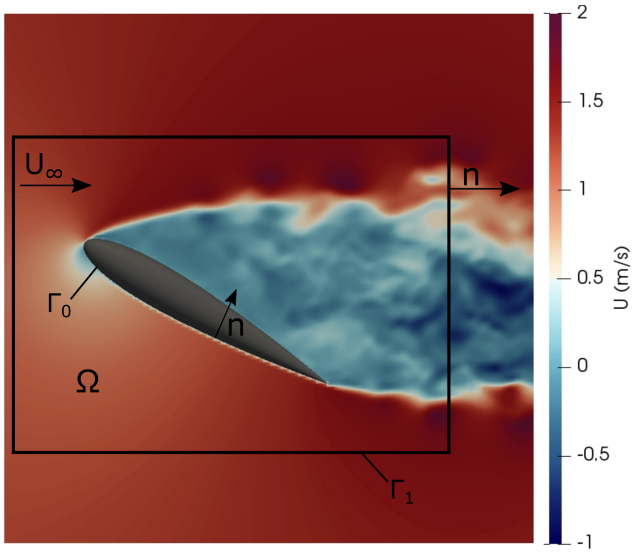


Fig. 1: Schematic of the problem set-up involving an object (a wing) with boundary $\Gamma_0$ placed in a flow with a free-stream velocity $U_\infty$. The control volume and its outer boundary are denoted $\Omega$ and $\Gamma_1$, respectively.

The unsteady and convective terms in (1) can be directly computed from the TR-PIV velocity flow fields. The third term requires calculation of the pressure along the control surface, which constitutes the main disadvantage of this method. The pressure can be obtained by spatially integrating the pressure gradient $\vec{\nabla}p$ which can be expressed in terms of the velocity field using the momentum equation

$$\vec{\nabla}p = -\rho\frac{D\vec{V}}{Dt} + \mu\vec{\nabla}^2\vec{V}. \tag{3}$$

Determination of pressure by numerical integration introduces inaccuracies coming from measurement errors and errors in the integration algorithm, both of which may render the results unreliable. In particular, while pressure must be available on the outer boundary $\Gamma_1$ only of the control volume, cf. equation (1) and Figure 1, which is an area where the velocity field can be measured relatively accurately, in the process one must evaluate second derivatives of the velocity field, cf. (3). Although practical methods for computing pressure from

the velocity fields have been recently significantly improved (Jeon et al., 2018), approaches to the determination of forces which do not require the demanding task of pressure computation will be more efficient.

### 2.2 Variational approach

Quartapelle & Napolitano (1983) proposed a variational approach to determine the instantaneous forces without calculating the pressure. This method is derived by expressing the pressure contribution to the force entirely in terms of the the velocity and vorticity fields. By definition, the pressure and viscous contribution to the force can be written on the body as:

$$\vec{F} = \vec{F}^P + \vec{F}^\mu = -\oint_{\Gamma_0} \left(-p\vec{n} + \bar{\bar{\tau}} \cdot \vec{n}\right)\, d\sigma. \tag{4}$$

Using vector-calculus identities and recognizing that the velocity field is divergence-free ($\vec{\nabla} \cdot \vec{V} = 0$), we obtain

$$\oint_{\Gamma_0} \left(\vec{\nabla}\vec{V}\right)^t \cdot \vec{n}\, d\sigma = \int_\Omega \vec{\nabla}\left(\vec{\nabla} \cdot \vec{V}\right)\, d\Omega = \mathbf{0}, \tag{5}$$

which allows us to transform expression (4) as follows (by adding a multiple of (5) to the second term)

$$\begin{aligned}
\vec{F} &= \oint_{\Gamma_0} \left[p\vec{n} - \mu\left(\vec{\nabla}\vec{V} + \left(\vec{\nabla}\vec{V}\right)^t\right) \cdot \vec{n}\right]\, d\sigma \\
&= \oint_{\Gamma_0} \left[p\vec{n} - \mu\left(\vec{\nabla}\vec{V} - \left(\vec{\nabla}\vec{V}\right)^t\right) \cdot \vec{n}\right]\, d\sigma \\
&= \oint_{\Gamma_0} \left[p\vec{n} + \mu\left(\vec{n} \times \vec{\omega}\right)\right]\, d\sigma.
\end{aligned} \tag{6}$$

Following the idea proposed by Quartapelle & Napolitano (1983), we will consider region $\Omega$ which corresponds to a control volume around the object. It is bounded by two surfaces: $\Gamma_0$ which coincides with the surface of the body, and $\Gamma_1$ which is the outer boundary, cf. Figure 1. Next, we introduce a harmonic function $\eta_x$ which depends only on the geometry of the region $\Omega$ and is defined through the following boundary-value problem for the Laplace equation

$$\Delta\eta_x = 0 \qquad \text{in } \Omega, \tag{7a}$$

$$\vec{n} \cdot \vec{\nabla}\eta_x = -\vec{e}_x \cdot \vec{n} \qquad \text{at } \Gamma_0, \tag{7b}$$

$$\vec{n} \cdot \vec{\nabla}\eta_x = 0 \qquad \text{at } \Gamma_1, \tag{7c}$$

where $\vec{e}_x$ is the unit vector associated with the $X$ axis. The function $\eta_x$ defined above is used for the determination of the $X$-component of the force. The functions $\eta_y$ and $\eta_z$, needed to determine the $Y$ and $Z$ components of the force, are defined by problems analogous to (7), but with the right-hand side of the boundary condition (7b) replaced with $-\vec{e}_y \cdot \vec{n}$ and $-\vec{e}_z \cdot \vec{n}$, respectively, where $\vec{e}_y$ and $\vec{e}_z$ are the unit vectors associated with the directions $Y$ and $Z$.

As shown below for the $X$ component of the force, introduction of the function $\eta_x$ defined as in (7) allows us to eliminate the pressure $p$ in terms of velocity in formula (6). First, an expression for the pressure gradient is obtained from the Navier-Stokes equations, cf. (3),

$$-\vec{\nabla}p = \rho\frac{\partial\vec{V}}{\partial t} + \rho\left(\vec{V} \cdot \vec{\nabla}\right)\vec{V} + \mu\vec{\nabla} \times \vec{\omega}, \tag{8}$$

where $\vec{\omega} = \vec{\nabla} \times \vec{V}$ is the vorticity. It is then projected, in the sense of the Hilbert space $L^2(\Omega)$ onto the gradient $\vec{\nabla}\eta_x$, i.e., the terms in equation (8) are multiplied by $\vec{\nabla}\eta_x$ and then integrated over $\Omega$ (Quartapelle & Napolitano, 1983; Protas et al., 2000). Integrating by parts, using the incompressibility constraint and the boundary conditions (7b)–(7c) for $\eta_x$, the following expression is derived for the pressure contribution to the $X$-component of the force $F_x^P = \oint_{\Gamma_0} (n_x p)\, d\sigma$, where $n_x = \vec{e}_x \cdot \vec{n}$, is derived

$$\begin{aligned}
F_x^P = \rho &\oint_{\Gamma_0\cup\Gamma_1} \eta_x\vec{n} \cdot \left(\frac{\partial\vec{V}}{\partial t}\right)\, d\sigma \\
&+ \mu \oint_{\Gamma_0\cup\Gamma_1} \vec{n} \cdot \left(\vec{\omega} \times \vec{\nabla}\eta_x\right)\, d\sigma \\
&+ \rho \int_\Omega \vec{\nabla}\eta_x \cdot \left[\left(\vec{V} \cdot \vec{\nabla}\right)\vec{V}\right]\, d\Omega.
\end{aligned} \tag{9}$$

Adding the contribution $F_x^\mu$ due to viscous stresses, equation (4) for the $X$-component of the force finally becomes

$$\begin{aligned}
F_x = &\rho \oint_{\Gamma_0\cup\Gamma_1} \eta_x\vec{n} \cdot \left(\frac{\partial\vec{V}}{\partial t}\right)\, d\sigma + \mu \oint_{\Gamma_0\cup\Gamma_1} \vec{n} \cdot \left(\vec{\omega} \times \vec{\nabla}\eta_x\right)\, d\sigma \\
&+ \rho \int_\Omega \vec{\nabla}\eta_x \cdot \left[\left(\vec{V} \cdot \vec{\nabla}\right)\vec{V}\right]\, d\Omega + \mu \oint_{\Gamma_0} \vec{e}_x\left(\vec{n} \times \vec{\omega}\right)\, d\sigma
\end{aligned} \tag{10}$$

and analogous expressions are obtained for the components $F_y$ and $F_z$.

The function $\eta_x$ is defined by problem (7) up to an arbitrary additive constant. However, as can be easily verified, the value of this constant does not have any effect on $F_x^P$ obtained in (9). Hence, without loss of generality, this constant can be set such that $|\eta_x| \to 0$ as $|\vec{x}| \to \infty$. Then, as can be deduced from the basic properties of the Laplace equation (7a), at large distances from the obstacle $|\vec{x}| \to \infty$ its solution and its

gradient vanish as (Protas et al., 2000)

$$|\eta_x| \sim \mathcal{O}\left(\frac{c}{|\vec{x}|}\right), \qquad \left|\vec{\nabla}\eta_x\right| \sim \mathcal{O}\left(\left(\frac{c}{|\vec{x}|}\right)^2\right) \quad \text{in 2D,} \tag{11a}$$

$$|\eta_x| \sim \mathcal{O}\left(\left(\frac{c}{|\vec{x}|}\right)^2\right), \quad \left|\vec{\nabla}\eta_x\right| \sim \mathcal{O}\left(\left(\frac{c}{|\vec{x}|}\right)^3\right) \quad \text{in 3D,} \tag{11b}$$

where $c$ is the cord length used here to represent the characteristic dimension of the object (the same estimates also apply to functions $\eta_y$, $\eta_z$ and their gradients). For simple obstacle geometries, such as a disk in 2D or a sphere in 3D, the functions $\eta_x$, $\eta_y$ and $\eta_z$ can be determined analytically (Protas et al., 2000). For more complicated geometries, problem (7) needs to be solved numerically, which is however quite straightforward and can be done using standard tools (such as the function `solvepde` in MATLAB).

As is evident from estimates (11), when the distance from the outer boundary $\Gamma_1$ to the obstacle increases, the relative contributions from the integrals defined on this boundary to (10) are reduced. In particular, in the limit when the outer boundary $\Gamma_1$ is pushed to infinity such that the control volume $\Omega$ coincides with the entire flow domain, the integrals on $\Gamma_1$ vanish altogether (Protas et al., 2000).

### 2.3 Validation against numerical data

In order to validate the proposed variational approach we use a numerical database obtained with an Improved Delayed Detached Eddy Simulation (IDDES) based on the formulation proposed by Shur et al. (2008). The code `StarCCM+` is used to carry out the simulations based on the k-omega-SST turbulence model. It is a widely used CFD code and general information about its validation in flows past airfoils can be found for example in Götten et al. (2019). A 3D flow around a rigid NACA0015 airfoil with an 80mm chord and 146mm span is considered. The wing has an angle of attack of 30 degrees and the upstream velocity is fixed at $U_\infty$=1.25m/s, resulting in a Reynolds number of $10^5$. The spatial resolution is 1mm in every direction near the wing and in the near wake, whereas the temporal resolution is 0.25ms. A hybrid second-order non-centered scheme is used in the RANS zone, changing to a centered scheme in the LES zone. In order to mimic an actual experiment, the velocity field is sampled on

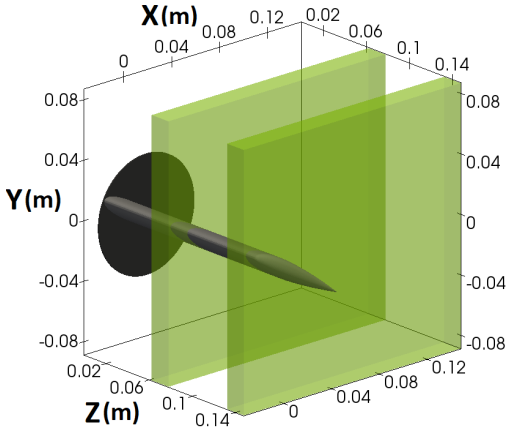


Fig. 2: Location of the two control volumes (represented by green rectangular boxes) with respect to the wing (represented by a dark slender object).

two Cartesian grids, cf. Figure 2, one at the wing mid-span with $Z = [0.06, 0.08]$m and another one at the wingtip with $Z = [0.13, 0.15]$m, where $Z$ is the spanwise coordinate. The spatial resolution is 1mm and the sampling rate 4000Hz. We refer the reader to Acher (2019) for further details concerning these computations, including validation tests and comparison to experimental data. We add that these calculations were also used by Gomit et al. (2018) to analyze the uncertainty of pressure estimation.

As explained Section 2.2, the functions $\eta_x$, $\eta_y$ and $\eta_z$ depend only on the geometry of the body, therefore they have to be determined for the objects tested. Figure 3 shows these functions in the exterior of the airfoil in the mid-span control volume considered here. We note that since the airfoil corresponds to the middle section of the wing, we have $\vec{e}_x \cdot \vec{n} = 0$ on $\Gamma_0$ and hence the function $\eta_z$ vanishes identically.

Once the functions $\eta_x$, $\eta_y$ and $\eta_z$ are determined, application of equation (10) to obtain the instantaneous force from the velocity and vorticity fields is in principle straightforward. However, the second term in equation (10) requires evaluation of the vorticity at the wing surface. In situations when the velocity field is sampled on Cartesian grids with modest resolution which are not well adapted to represent curved boundaries this may lead to significant inaccuracies in the evaluation of the velocity derivatives, and this problem is illustrated in Figure 4. To address this issue, an irregular body-fitted grid around the wing is generated. Then, the velocity field is interpolated onto this new grid to obtain considerably more accurate spatial derivatives at the wing surface. For the spatial derivative in the direction normal to the wing surface, a non-centered second-order discretization scheme is used, while for the spatial derivative in the direction tangent to the wing

surface, a centered second-order discretization scheme is used, and these schemes are shown in equations (12) and (13), respectively.

$$\frac{\partial u^n}{\partial x_i} = \frac{-3u_i^n - u_{i+2}^n + 4u_{i+1}^n}{2\Delta x} + \mathcal{O}\left(h^2\right), \tag{12}$$

$$\frac{\partial u^n}{\partial x_i} = \frac{u_{i+1}^n - u_{i-1}^n}{2\Delta x} + \mathcal{O}\left(h^2\right). \tag{13}$$

The process of interpolating the velocity field from a Cartesian grid to a boundary-fitted grid in the neighborhood of the wing and the resulting vorticity field obtained on this grid are shown in Figures 5 and 6, respectively. Then, equation (10) can be applied using these velocity and vorticity fields to determine the force acting on the wing. We note that that the first term in equation (10) involves a time derivative which is approximated using 3 consecutive instantaneous fields sampled at the rate of 4000Hz. The accuracy of the proposed approach is assessed in the next section.

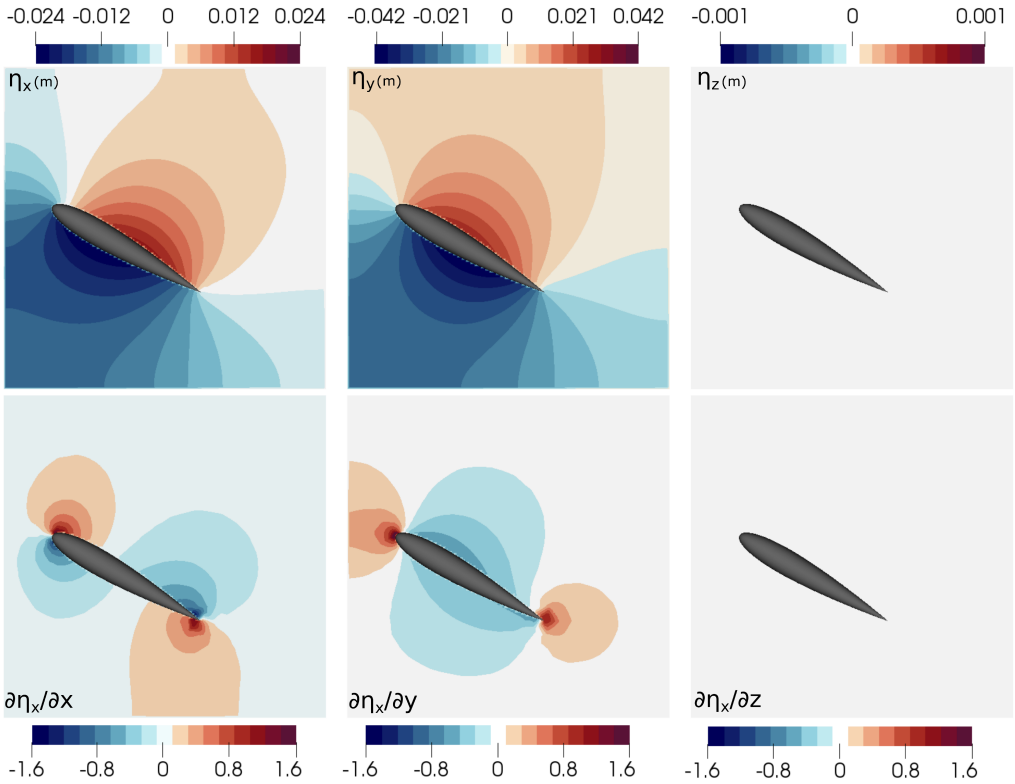


Fig. 3: Harmonic functions $\eta_x$, $\eta_y$ and $\eta_z$ (top row) and three components of the gradient $\vec{\nabla}\eta_x$ (bottom row) in the control volume at the wing mid-span, cf. Figure 2, characterizing the relative influence of the flow field in the different parts of the flow domain on the hydrodynamic force.

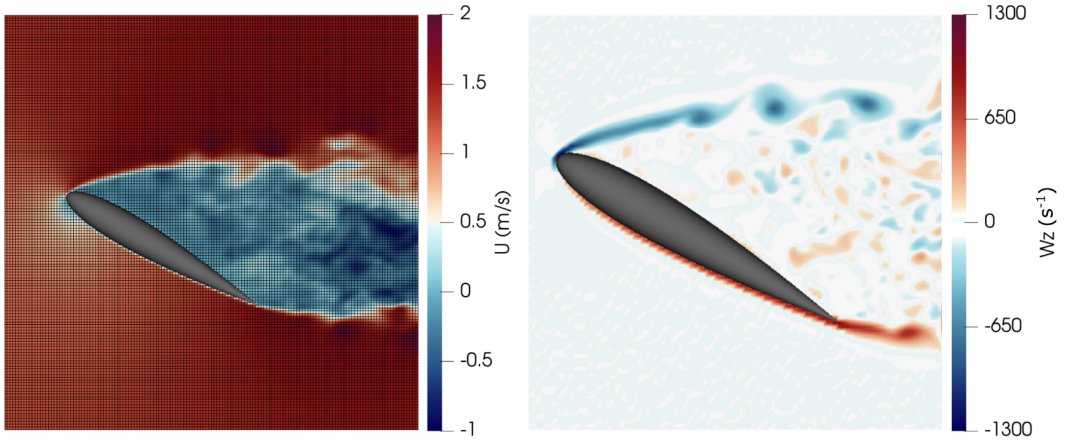


Fig. 4: The horizontal component of the velocity field on the Cartesian grid (left) and a magnification of the spanwise component of the corresponding vorticity field (right).

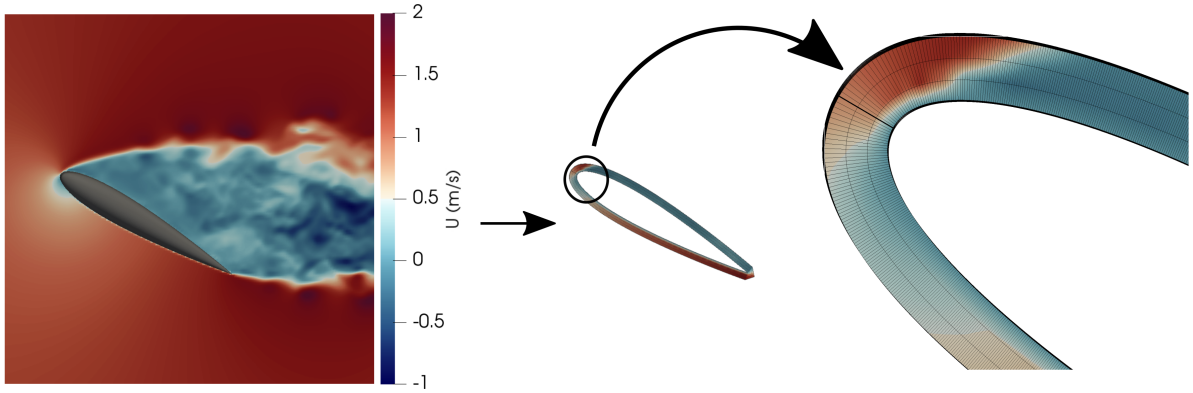


Fig. 5: Schematic showing the interpolation of the velocity field onto a refined boundary-fitted grid around the wing to obtain a more accurate vorticity field on the surface.

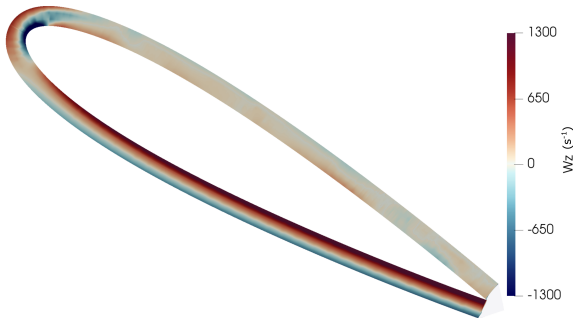


Fig. 6: The spanwise component of the vorticity field obtained from the velocity field interpolated onto a boundary-fitted grid in the neighborhood of the wing.

## 3 Results and comparisons

### 3.1 Comparison criterion

The results obtained with the momentum equation and the variational method using different sets of parameters are now compared against the force obtained directly from the numerical simulations described in Section 2.3, which is considered as the reference, in terms of the following relative errors

$$\epsilon_x = \frac{|F_x^e - F_x^n|}{F_x^n}, \quad \epsilon_y = \frac{|F_y^e - F_y^n|}{F_y^n}, \tag{14}$$

where the superscripts "$e$" and "$n$" refer to the estimated force and its reference value obtained from the numerical database. Given the required computational cost, our analysis here is first focused on instantaneous values of the force components which fluctuate in time given the unsteady nature of the flow. However, the magnitude of the errors in the two methods was found to remain of the same order at a number of different time instances, such that representative results can be obtained by considering a single instant of time. We note that the results presented in Sections 3.2–3.5 are based on data obtained from the numerical simulations discussed in Section 2.3 and corresponding to the control volume at midspan, cf. Figure 2, whereas experimental data obtained in a control volume at the wingtip is used in Section 3.6. That section will also feature results for the mean forces.

### 3.2 Sensitivity to the control volume

The variational formula (10) involves integrals defined on the outer boundary $\Gamma_1$ which depend on the values of the vorticity $\vec{\omega}$ and acceleration $\partial\vec{V}/\partial t$, the latter of which may be especially difficult to approximate accurately based on the experimental data. On the other hand, these integrals also involve rapidly decaying factors given by the functions $\eta_x$ and $\vec{\nabla}\eta_x$, cf. Figure 3, such that it may be expected that the contribution provided by these integrals to the total force will vanish as $\Omega$ becomes larger and $\Gamma_1$ is removed further away from the obstacle. In this section we thus assess the effect of the size of the control volume $\Omega$ on the accuracy of the forces evaluated using the variational formula (10).

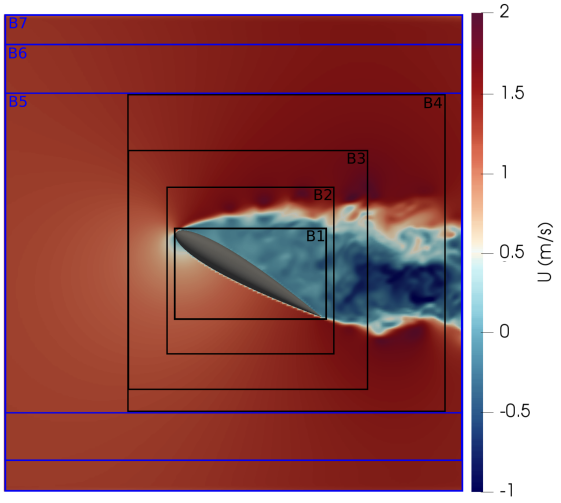


Fig. 7: Different control volumes used as region $\Omega$ in the variational approach.

Table 1: Instantaneous drag and lift forces computed using the variational formula (10) and the control volumes shown in black in Figure 7 together with the corresponding errors and control volume sizes $(\Delta x, \Delta y)$ expressed in terms of the cord length $c$. Errors considered acceptable are marked in blue, whereas red corresponds to excessive error levels (this convention applies to all tables).

| Variable | Reference | B1 | B2 | B3 | B4 |
|---|---|---|---|---|---|
| $F_x(N)$ | 0.520 | 0.3120 | 0.7481 | 0.5357 | 0.5204 |
| $\epsilon_x$ | | **39.95%** | **43.99%** | **3.11%** | **0.17%** |
| $F_y(N)$ | 0.760 | 0.6107 | 0.9512 | 0.6466 | 0.6818 |
| $\epsilon_y$ | | **19.62%** | **25.19%** | **14.90%** | **10.27%** |
| $\Delta x$ | | 0.9125c | 1c | 1.4c | 1.85c |
| $\Delta y$ | | 0.55c | 1c | 1.4c | 1.85c |

In Table 1 we report the instantaneous drag and lift forces computed using the control volumes of increasing size expressed in terms of the chord length $c$, cf. black rectangles in Figure 7, together with the corresponding errors. As is evident from this table, as the size of the control volume increases, the errors in the evaluation

of the force decrease becoming smaller than 1% for the drag and about 10% for the lift component.

In order to provide a comprehensive assessment of the effect of the shape of the control volume and of its orientation with respect to the obstacle, we computed the force using additional control volumes shown in blue in Figure 7. The results are reported in Table 2. We see that extending the control volume in the longitudinal direction and progressively moving the lateral boundaries away from the body allows us to further reduce the errors in the evaluation of the drag component (the effect is negligible for lift which is already determined quite accurately). This observation can be attributed to the fact that inaccuracies in the evaluation of the integrals on $\Gamma_1$ can be mitigated by removing the boundary of the control volume further away from the obstacle, such that the contributions of these integrals to the total force are smaller because of the rapid decay of $\eta_x$ and $\vec{\nabla}\eta_x$ as $|\vec{x}|\to\infty$, cf. (11). However, even for the largest considered control volumes the distance from the outer boundary $\Gamma_1$ to the obstacle was not large enough for the integrals defined on $\Gamma_1$ to be neglected.

Table 2: Instantaneous drag and lift forces computed using the variational formula (10) and the control volumes shown in blue in Figure 7 together with the corresponding errors and control volume sizes $(\Delta x, \Delta y)$ expressed in terms of the cord length $c$. The data in the table corresponds to a different time instant than the data in Table 1, so the reference values of the force components are slightly different.

| Variable | Reference | B5 | B6 | B7 |
|---|---|---|---|---|
| $F_x(N)$ | 0.5149 | 0.4706 | 0.4914 | 0.5030 |
| $\epsilon_x$ | | **8.67%** | **4.91%** | **2.31%** |
| $F_y(N)$ | 0.7672 | 0.7773 | 0.7761 | 0.7865 |
| $\epsilon_y$ | | **1.32%** | **1.16%** | **2.52%** |
| $\Delta x$ | | 2.725c | 2.725c | 2.725c |
| $\Delta y$ | | 1.85c | 2.475c | 2.875c |

### 3.3 Comparison of the two approaches

A comparison of the results obtained from the variational method for our unsteady 3D test case with the well-known momentum equation approach is now presented. As regards the latter approach, cf. (1), the derivative terms in the integrand expressions representing the unsteady, convective and viscous effects are computed directly from the velocity fields using centered second-order finite-difference schemes. The third term in (1) requires calculation of the pressure along the control surface $\Gamma_1$ which can be done by spatially integrating the pressure gradient $\vec{\nabla}p$ as described in Jeon et al. (2018). The different terms in (3) are calculated from the velocity fields using centered second-order finite-difference schemes. The pressure field is then determined by minimizing a functional defined as the difference between the pressure gradient based on the measurements and the estimated pressure gradient, which is equivalent to solving the Poisson equation and provides a more robust approximation of the pressure field. This field is generally divided into subdomains based on the amplitude of the pressure gradient. The sequential pressure reconstruction is initiated from the outer domain, where the highest measurement accuracy is expected, such that a reliable pressure reference can be established. The pressure field in the other subdomains is then computed by imposing Dirichlet boundary conditions deduced from the values of the pressure on the previously computed outer domains. We refer the reader to Jeon et al. (2018) and Gomit et al. (2018) for further details of this approach as well as for analysis of its performance and parameter sensitivity.

Table 3 shows that errors obtained with both methods are of the same order. This means that the choice of one approach over the other should be based on which is more suitable for the specific problem at hand, bearing in mind that for the variational method a sufficiently accurate vorticity field is required at the surface of the body, whereas for the momentum equation approach the computation of the pressure is needed. However, other aspects such as the sensitivity to spatial resolution and noise of both methods should also be taken into account, as discussed in the next section.

Table 3: Instantaneous drag and lift forces based on the variational formula (10) and the momentum equation (1) using the control volume B7, cf. Figure 7, together with the corresponding errors.

| Variable | Variational method (B7) | Momentum eq. approach |
|---|---|---|
| $F_x(N)$ | 0.5030 | 0.5226 |
| $\epsilon_x$ | **2.31%** | **1.49%** |
| $F_y(N)$ | 0.7865 | 0.7475 |
| $\epsilon_y$ | **2.52%** | **2.57%** |

### 3.4 Sensitivity to spatial resolution

Since high resolution is not always available in experiments, in this section we study how the accuracy of the two considered methods depends on this parameter.

Table 4: Errors in the evaluation of instantaneous forces obtained with the variational and the momentum equation approach for different spatial resolutions given in terms of grid spacing.

| Resolution | Variable | Variational method (B7) | Momentum eq. approach |
|---|---|---|---|
| (1,1,1)mm | $\epsilon_x$ | 2.31% | 1.49% |
| (=0.0125c) | $\epsilon_y$ | 2.52% | 2.57% |
| (2,2,2)mm | $\epsilon_x$ | **26.04%** | **0.09%** |
| (=0.025c) | $\epsilon_y$ | **18.66%** | **6.44%** |
| (4,4,2)mm | $\epsilon_x$ | **25.05%** | **0.63%** |
| (=0.05c) | $\epsilon_y$ | **15.11%** | **3.16%** |

Table 4 presents the results obtained for different spatial resolutions indicating that the variational approach appears highly sensitive to this parameter. This can be explained by the presence of a boundary integral defined on the surface of the obstacle and involving vorticity which cannot be evaluated accurately, unless sufficiently refined resolution is used. On the other hand, the momentum equation approach demonstrates much better results with lower spatial resolution.

### 3.5 Sensitivity to noise

Since all measurements are to various degrees contaminated by noise, we now assess how this factor affects the accuracy of force evaluations. To this end, additive Gaussian noise is introduced in the numerical velocity fields used for the determination of the forces. Is is constructed as a random variable with the probability density function

$$\Pr(E_r) = \frac{1}{\sqrt{2\pi\sigma}} e^{-\frac{(E_r-\mu)^2}{2\sigma^2}} \tag{15}$$

where $\mu$ is the mean value and $\sigma$ the standard deviation of the error $E_r$. This noise is generated randomly over all discrete points in the field, independently of their position or velocity, and its level is chosen to match the noise levels typically encountered in PIV measurements. Thus, the noise has zero mean and its standard deviation is defined in terms of the voxel error (particle-image displacement) as described by Gomit et al. (2018). The lowest noise level corresponds to $3\sigma = 0.05vx$ and the highest level to $3\sigma = 0.5vx$ with several values in between. In terms of the velocity magnitude, these values correspond to $3\sigma_u = 0.012m.s^{-1}$ (1% of $U_\infty$) and $3\sigma_u = 0.12m.s^{-1}$ (10% of $U_\infty$), respectively. For each value of $\sigma$ the mean error in the evaluation of the force is then obtained by averaging over 20 noise samples and is shown as a function of $\sigma$ for the two methods in Figures 8 and 9 for the drag and lift component, respectively.

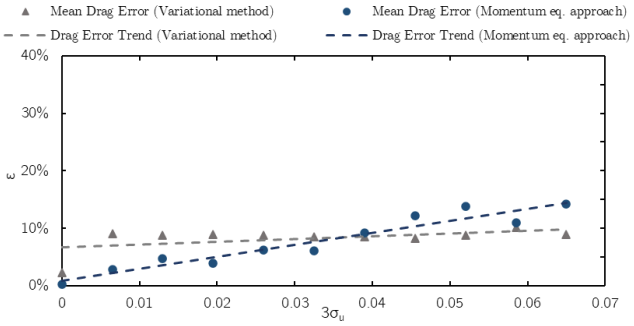


Fig. 8: Error in the evaluation of the drag component with the two methods as a function of the noise level.

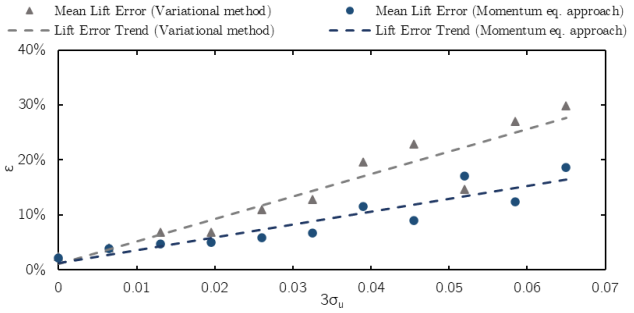


Fig. 9: Error in the evaluation of the lift component with the two methods as a function of the noise level.

In Figure 8 we see that, interestingly, the drag component computed based on the variational approach appears insensitive to the noise level, in contrast to the error in the momentum-equation approach which tends to increase in proportion to the noise level $\sigma$. Thus, as a result, the variational approach offers a more robust way to compute the drag when large noise is present. On the other hand, the error in the lift component, cf. Figure 9, computed with the two approaches increases in proportion to the noise level and tends to be higher by a factor of approximately 2 in the case of the variational approach.

### 3.6 Application to experimental data

To complete the analysis, both approaches are tested using experimental data obtained by Acher et al. (2019) in the same setup and for the same flow configuration involving a rigid wing with a NACA0015 airfoil as was studied numerically in Section 2.3. Tomo-PIV measurements provide the flow fields around the wing with a spatial resolution of 1.6 mm (which is between the intermediate and the refined resolutions studied in Table 4) in all three dimensions and sampled over the two

control volumes shown in Figure 2. A scale at the base of the wing allowed for a direct measurement of the total forces experienced by the wing. Although the force measurements were not simultaneous with the Tomo-PIV measurements, these results made it possible to validate the numerical simulations. However, since the PIV data is acquired in a thin section of the wing whose contribution to the total forces cannot be determined experimentally, cf. Figure 2, the relative errors (14) are still computed with reference to the numerically evaluated force components.

Due to the setup of the experiments, the flow near the wing surface is not well resolved in the control volume located at the mid-span of the wing, cf. Figure 10. The reason is that the shadow of the wing obscures the region under the wing intrados, impeding the acquisition of the velocity field in this area. On the other hand, the control volume located at the wingtip does not present this visualization problem and the flow field can be acquired in that region, cf. Figure 11.

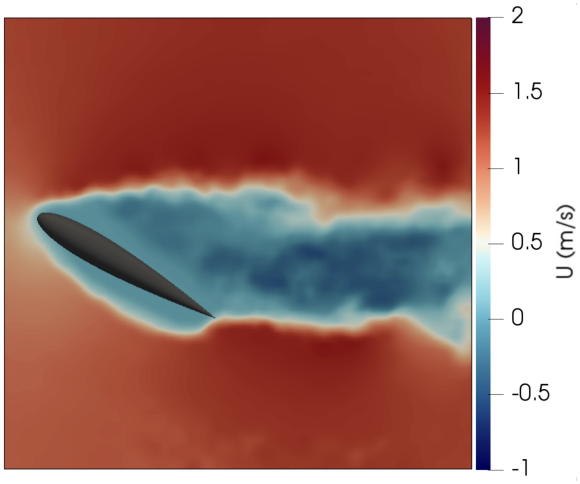


Fig. 10: The experimental velocity field (the horizontal component) obtained from Tomo-PIV measurements in the control volume at the mid-span of the wing, cf. Figure 2.

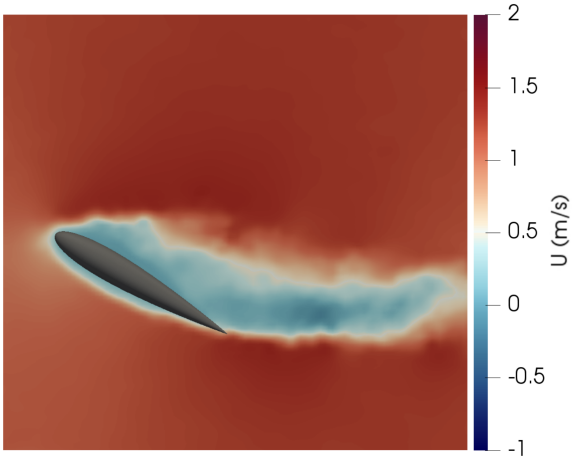


Fig. 11: The experimental velocity field (the horizontal component) obtained from Tomo-PIV measurements in the control volume at the wingtip, cf. Figure 2.

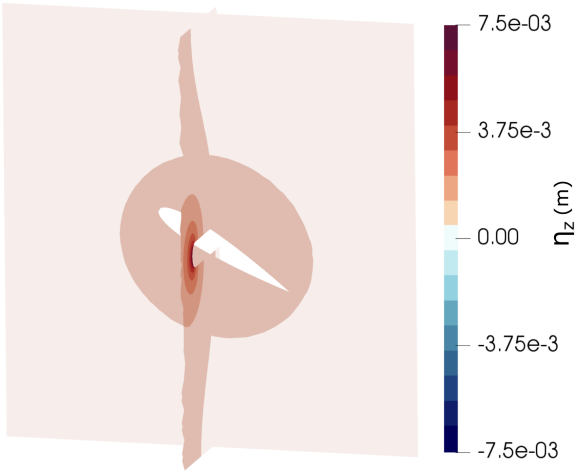


Fig. 12: The function $\eta_z$ defined in the control volume at the wingtip.

Thus, since the flow field in the control volume at the mid-span of the wing does not make it possible to determine the vorticity at the wing surface with sufficient accuracy for the application of the variational method, the control volume at the tip of the wing is the one used for the force evaluation. However, we notice that the $Z$-component of the normal vector $\vec{n}$ at the wing surface $\Gamma_0$ is no longer zero for this control volume and therefore the function $\eta_z$ does not vanish identically in this case, cf. Figure 12.

Following the same procedure as used for the numerical data in Section 2.3, the vorticity around the wing is calculated on a body-fitted refined grid and the functions $\eta_x$, $\eta_y$ and $\eta_z$ are determined for the new control volume. Results of the application of the two approaches are summarized in Table 5 where we observe

that both approaches produce very similar instantaneous values of the force components.

Table 5: Instantaneous drag and lift forces computed based on the variational formula (10) and the momentum equation (1) using the experimental data.

| Instant | Variable | Variational method | Momentum eq. approach |
|---|---|---|---|
| 1 | $F_x(N)$ | 0.1503 | 0.1699 |
| 1 | $F_y(N)$ | 0.1846 | 0.1869 |
| 2 | $F_x(N)$ | 0.1196 | 0.1190 |
| 2 | $F_y(N)$ | 0.2126 | 0.1854 |

Table 6: Mean drag and lift forces and their STD values computed based on the variational formula (10) and the momentum equation (1) using the experimental data together with the corresponding errors with respect to the numerical data.

| Variable | Numerical reference | Variational method | Momentum eq. approach |
|---|---|---|---|
| $\overline{F_x}(N)$ | 0.1591 | 0.1315 | 0.1148 |
| $\epsilon_x$ | | **17.34%** | **27.84%** |
| $\overline{F_y}(N)$ | 0.1996 | 0.2014 | 0.1813 |
| $\epsilon_y$ | | **0.91%** | **9.17%** |
| $F_{\mathrm{x}}^{\mathrm{STD}}\ (N)$ | 0.1592 | 0.1417 | 0.1514 |
| $\epsilon_{\mathrm{x}}^{\mathrm{STD}}$ | | **10.94%** | **4.84%** |
| $F_{\mathrm{y}}^{\mathrm{STD}}\ (N)$ | 0.1997 | 0.2031 | 0.1971 |
| $\epsilon_{\mathrm{y}}^{\mathrm{STD}}$ | | **1.70%** | **1.30%** |

However, a more realistic view of the performance of the two methods can be given by computing the mean forces together with their standard deviations (STD) instead of just the instantaneous values. Table 6 shows these results for the drag and lift components obtained by averaging 120 instantaneous force values sampled at the rate of 40Hz. The total window of 3 seconds is short, but nonetheless allows us to detect trends. These results are compared against the mean and STD values obtained from the numerical simulations and used as reference, keeping in mind they also involve certain errors.

Most of the results in Table 6 show an error below 12%, but the one found for the mean drag force is significantly higher. Errors found in the momentum equation approach mostly come from noise in the experimental data. On the other hand, the variational approach produces slightly better results with errors below 18%. However, in this case the main source of error appear to be the inaccuracies in the evaluation of the integrals defined on the outer surface $\Gamma_1$ whose relative contributions to the total force diminish as the size of the control volume increases (cf. Section 2.3) as well as the limitation due to the spatial resolution. Nevertheless, we should also keep in mind that the flow is at a Reynolds number of $10^5$ and the control volume tested is at the wingtip, where the three-dimensional effects are particularly important and larger inaccuracy is expected. In addition, as is evident from the results presented in Figures 8 and 9, an error of 15 to 25% can be expected when taking into account noise in the flow field.

Therefore, in the light of the results discussed in Section 3.4, cf. Table 4, we can conclude that when experimental flow fields are used, the spatial resolution of 1.6mm is sufficient for the variational approach to provide results that are practically as accurate as the ones obtained with the momentum equation approach. Then, if the pressure field around the object is not required and the vorticity field can be reliably determined at the object surface, the computational cost to determine the forces can be significantly reduced with the variational method. On the other hand, the momentum equation approach remains the best choice when access to the near-wall fields is limited in experimental measurements.

## 4 Conclusions

The variational approach, first proposed by Quartapelle & Napolitano (1983) and then elaborated by Protas et al. (2000), was applied to determine the hydrodynamic force in a 3D unsteady flow computed numerically and studied experimentally. The main advantage of this method resides in not requiring the computation of the pressure field around the object to determine the forces. However, an accurate vorticity field is needed at the surface of the body to have reliable results (it was proved by Protas (2007) that the contribution from the vorticity at the boundary cannot be in fact eliminated in this approach). While the variational approach has been employed before in numerical studies, the present investigation is to the best of our knowledge its first application to experimental data.

The momentum equation approach, another non-intrusive method to determine forces, was also applied to our test cases to allow for a performance comparison between the two techniques. The results in the numerical cases show that both methods are able to obtain the forces around the tested wing with an error of less than 3%. Therefore, it is more convenient to apply the variational method in situations where the position of the object is known accurately making it possible to obtain sufficiently accurate vorticity fields at the wing surface while not requiring the computation of the pressure. On the other hand, when the vorticity at the wing surface cannot be obtained with enough accuracy, the momentum equation approach is more suitable and the pressure will need to be computed.

The sensitivities of the two approaches to the spatial resolution of the measurements and the measurement noise were also assessed. The spatial resolution has a direct effect on the accuracy of the vorticity field calculated at the wing surface and we showed that for lower spatial resolutions the variational approach does not provide reliable results, while the momentum equation approach tends to produce results within 10% error regardless of the resolution. On the other hand, our results also show that the variational approach can be less sensitive to noise than the momentum equation approach.

Finally, we applied both methods to experimental flow fields obtained in the same conditions as used in the numerical tests. The results showed that in this case, for a spatial resolution of 1.6mm, the variational approach can provide results that are as good as those obtained with the momentum equation approach.

In summary, both approaches have certain advantages and limitations — the variational approach requires the vorticity field to be available on the surface of the obstacle, whereas in the approach based on the momentum equation pressure is needed on the outer boundary $\Gamma_1$ of the control volume. While this quantity can in practice be deduced from the velocity fields measured away from the obstacle in a straightforward manner, this advantage is offset by the fact that in the process one must evaluate the second derivatives of the velocity field, cf. (3); in contrast, only first derivatives of the velocity field are required in the variational approach, cf. (10). We thus conclude that, if the pressure field around the object is not required and the vorticity field can be reliably determined at the surface of the obstacle, the computational cost to determine the forces can be significantly reduced with the variational method. On the other hand, the momentum equation approach remains the method of choice when the near-wall field cannot be easily measured in experiments.

There are some open problems related to the variational approach that will benefit from additional research. One is to understand why the drag and lift components computed in this way exhibit different levels of sensitivity to noise, cf. Figures 8 and 9. Another would be to develop a systematic approach to find an optimal shape and size of the control volume that would minimize different errors for a given flow configuration.

**Acknowledgements** The authors are grateful to an anonymous referee for constructive feedback which helped improve the presentation of the results. The current work has been conducted as part of the EVAPOR Astrid project, funded by the Agence Nationale de la Recherche and the DGA, Grant No. NR-16-ASTR-0005-01 and the CPER FEDER project of the Nouvelle Aquitaine Region. BP acknowledges partial support through an NSERC Discovery Grant.

## References

Acher G (2019) Couplage de mesures de vitesse par Tomo-PIV et de déformation de profil, pour l'étude des interactions fluide-structure. Ph.D. Thesis, Universite de Poitiers.

Acher G, Thomas L, Tremblais B, Gomit G, Chatellier L, and David L (2019) Simultaneous measurements of flow velocity using Tomo-PIV and deformation of a flexible wing. In Proceedings of the 13th International Symposium on Particle Image Velocimetry, Munich.

Chang, C-C, (1992) Potential flow and forces for incompressible viscous flow. Proceedings of the Royal Society A 437, 517–525.

Chang, C-C, Lei, S-Y, (1996) On the sources of aerodynamic forces: steady flow around a cylinder or a sphere. Proceedings of the Royal Society A 452, 2369–2395.

Chang, C-C, Su, J-Y, Lei, S-Y, (1998) On aerodynamic forces for viscous compressible flow. Theoretical and Computational Fluid Dynamics 10, 71–90.

David L, Jardin T, and Farcy A (2009) On the non-intrusive evaluation of fluid forces with the momentum equation approach. Meas Sci Technol 20(9), 095401

Gomit G, Acher G, Chatellier L and David L (2018) Uncertainty analysis of an optical method for pressure estimation in fluids. Meas Sci Technol 29(2), 024004

Götten F, Finger F, Havermann M, Braun C, Marino M, Bil C (2019) A highly automated method for simulating airfoil characteristics at low Reynolds number using a RANS — transition approach. Deutscher Luft- und Raumfahrtkongress 2019 DocumentID: 490026.

Howe, M S (1995) On the force and moment on a body in an incompressible fluid, with application to rigid bodies and bubbles at high and low Reynolds numbers. Quarterly Journal of Mechanics and Applied Mathematics 48, 401–426.

Jardin T, Chatellier L, Farcy A, David L (2009) Correlation between vortex structures and unsteady loads for flapping motion in hover. Exp Fluids 47, 655–664

Jeon Y J, Gomit G, Earl T, Chatellier L, and David L (2018) Sequential least-square reconstruction of instantaneous pressure field around a body from TR-PIV. Exp Fluids 59(2), 27

Kurtulus D F, Scarano F, and David L (2007) Unsteady aerodynamic forces estimation on a square cylinder by TR-PIV. Exp Fluids 42(2), 185-196

Lighthill J (1986) Fundamentals concerning wave loading offshore structures. J Fluid Mech 173:667-681

Limacher E, McClure J, Yarusevych S and Morton C (2020) Comparison of momentum and impulse formulations for PIV-based force estimation. Meas Sci Technol 31(5), 054001

Lin J C, and Rockwell D (1996) Force identification by vorticity fields: techniques based on flow imaging. J Fluids Struct 10:663-668

Noca F, Shiels D, and Jeon D (1997) Measuring instantaneous fluid dynamic forces on bodies, using only velocity fields and their derivatives. J Fluids Struct 11:345-350

Noca F, Shiels D, and Jeon D (1999) A comparison of methods for evaluating time-dependent fluid dynamic forces on bodies, using only velocity fields and their derivatives. J Fluids Struct 13:551-578

Pan, L S, Chew, Y T, (2002) A general formula for calculating forces on a 2–D arbitrary body in incompressible flow. Journal of Fluids and Structures 16, 71–82.

Protas B, Styczek A, and Nowakowski A (2000) An Effective Approach to Computation of Force in Viscous Incompressible Flows. J Comput Phys 159:231-245

Protas B (2007) On an Attempt to Simplify the Quartapelle-Napolitano Approach to Computation of Hydrodynamic Forces in Open Flows. J Fluids Struct 23(8), 1207-1214

Quartapelle L, and Napolitano M (1983) Force and moment in incompressible flows. AIAA J 21:911-913

Shur M L, Spalart P R, Strelets M K, and Travin A K (2008) A hybrid RANS-LES approach with delayed-DES and wall-modelled LES capabilities. Int J Heat Fluid Flow 29(6), 1638-1649

Unal M F, Lin J C and Rockwell D 1997 Force prediction by PIV imaging: a momentum based approach J. Fluids Struct. 11 965–71

Van Oudheusden B W, Scarano F, and Casimiri E W (2006) Non-intrusive load characterization of an airfoil using PIV. Exp Fluids 40:988-992